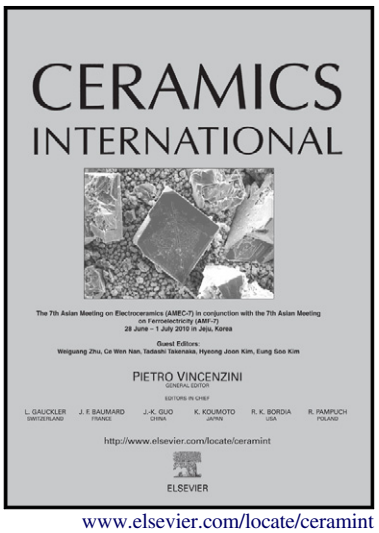

www.elsevier.com/locate/ceramint

Effect of functionalisation of CNT in the preparation of HAp-CNT biocomposites

Susmita Mukherjee, Biswanath Kundu, Abhijit Chanda, Swarnendu Sen

PII: S0272-8842(14)01790-8
DOI: http://dx.doi.org/10.1016/j.ceramint.2014.11.052
Reference: CERI9497

To appear in: *Ceramics International*

Received date: 31 July 2014
Revised date: 30 October 2014
Accepted date: 6 November 2014

Cite this article as: Susmita Mukherjee, Biswanath Kundu, Abhijit Chanda, Swarnendu Sen, Effect of functionalisation of CNT in the preparation of HAp-CNT biocomposites, *Ceramics International,* http://dx.doi.org/10.1016/j.ceramint.2014.11.052

Effect of functionalisation of CNT in the preparation of HAp-CNT biocomposites

Susmita Mukherjee*, Biswanath Kundu[1, **], Abhijit Chanda[2], Swarnendu Sen[2]

School of Materials Science and Nanotechnology, Jadavpur University, Kolkata 700032, India

[1] Bioceramics and Coating Division, CSIR-Central Glass and Ceramic Research Institute, Kolkata 700032, India

[2] Department of Mechanical Engineering, Jadavpur University, Kolkata 700032, India

* 1st corresponding author; Email: susm08@gmail.com, Phone: +91-9674459006

** 2nd corresponding author; Email: biswa_kundu@rediffmail.com, Phone: +91-9831772081

Abstract

Hydroxyapatite (HAp)-carbon nanotube (CNT) composites are being fabricated, where CNT acts as a reinforcement in the ceramic matrix. CNT improves the mechanical property of HAp and offers a potential implant material used for orthopedic applications. In the present work, a comparative study is presented to analyse the effect of functionalisation on the properties of HAp-CNT nanocomposites, prepared by a simple shear mixing technique. The MWCNT chains were functionalised with carboxyl groups, confirmed through FTIR spectra. FESEM and TEM results of the composites showed that for non functionalised chains, CNT molecules were present in sporadic clusters while the functionalised chains were found to be dispersed in the HAp matrix. Fractographs exhibited the presence of CNT chains acting as bridges across the cracks. Nanocomposites with functionalised CNT molecules exhibited better mechanical properties compared to non functionalised ones as revealed through HV, K_{1c}, nano-indentation H and E estimation, flexural and compressive strength and impact resistance. This superiority of composite specimens may be attributed to the crack bridging action of the CNT. Both the composites exhibited excellent haemocompatibility and incorporation of CNT molecules and functionalisation did not affect this.

Keywords: Hydroxyapatite; carbon nanotube; nanocomposites; functionalisation; haemocompatibility

1. Introduction

In order to meet the growing demand for orthopedic implants, there has been an urgent need to develop synthetic biomaterials for bone replacement applications, as autografts and allografts have their own set of drawbacks. calcium phosphate materials with their high biocompatibility, form the key structural material for natural bone and teeth [1]. Among the different forms of calcium phosphates, hydroxyapatite (HAp) has been widely used as a bone reconstruction material owing to its compositional similarity [$Ca_{10}(PO_4)_6(OH)_2$], crystal structure and Ca:P ratio (1.67) as found in the apatite of human skeletal system. Despite their excellent biocompatibility, osteoconductivity and bone-bonding property, inherent brittleness and low fracture toughness of the HAp ceramics impedes their usage for direct load bearing applications. Pure HAp with a low toughness (0.8-1.2 MPa $m^{1/2}$) and poor flexural strength (< 140 MPa) as compared to human bone [2], finds applications either as a coating on different implants like steel, titanium, titanium alloy [3] or as a scaffold for tissue engineering [4]. In order to improve the mechanical property, associated literatures also reported reinforcement of HAp ceramics with different materials like zirconia, glass, silver, alumina, titania, carbon fiber and carbon nanotubes [5-8].

Carbon nanotubes (CNTs), the quintessential nanomaterials, possess a combination of excellent mechanical, structural, electrical, thermal and chemical properties [9-11] and can be used as an outstanding reinforcement material for HAp. In multiwalled carbon nanotubes (MWCNT), multiple graphene layers are arranged concentrically at an interlayer distance of 0.3-0.4 nm and held together by van de Waals attractions. Rouff et al proposed that when used in a composite, fracture occurs via collapse of the inner walls of CNT molecules, thereby providing extra absorption energy and increasing the toughness of the composite [12]. At low loadings, CNTs can successfully impart mechanical integrity to the HAp matrix, without affecting its bioactivity.

The inherent van der Waals interaction between the nanotube walls keeps them as aggregated bundles in their native state, renders the CNT chains poor solubility and processability that act as main obstacle for their usage in different applications [13, 14]. Side chain functionalisation improves their solubility by attaching functional groups on their surface [14]. Introduction of various functional groups on the surface reduces the inter chain interactions and enhances their

dispersability in solution or composite materials. A variety of functional groups or molecules can be introduced through further chemical modification of these functionalised CNTs [15, 16].

The present work portrays a comparative study of the pristine non-functionalised (n-CNT) and functionalised (f-CNT) carbon nanotubes in the synthesis of the HAp-CNT nanocomposites. Our basic objective is to understand the effect of functionalisation on the mechanical and biological properties of the composites. Composites were prepared using a cost effective shear mixing technique with different proportions of CNT and the effect of the reinforcement were investigated.

2. Materials and methods

In the present work, multiwalled carbon nanotubes (MWCNT, purity > 95%, average diameter of 10-30 nm and average length of 1-10 μm), were procured from Nanoshel LLC, USA while the HAp powder was synthesized in the laboratory.

2.1. Synthesis of HAp powders

HAp powder was prepared in the laboratory using the precipitation method [17]. Analytical grade ortho-phosphoric acid (H_3PO_4) and calcium hydroxide, $Ca(OH)_2$ (S.D. Fine Chem Ltd., India) were used as the starting reagents:

$$10\ Ca(OH)_2 + 6H_3PO_4 = Ca_{10}(PO_4)_6(OH)_2 + 18H_2O$$

Details of the procedure and characterisation adopted have been discussed elsewhere [18]. Very briefly, an aqueous solution of H_3PO_4 was slowly added to $Ca(OH)_2$ solution, the molar concentration of the precursors was adjusted to have a theoretical Ca/P ratio of 1.67. The reaction was carried out with continuous stirring, at a temperature of 80 °C and pH of 11-12. The resultant white precipitate was aged, dried at 70 °C and finally calcined at 800 °C for 2 h.

2.2. Functionalisation of the MWCNT

The as-received MWCNTs were treated with a mixture of concentrated H_2SO_4 and concentrated HNO_3 (3:1, by volume). The mixture was stirred ultrasonically for 3 h at ambient temperature

and kept for another 8-9 h. The black suspension was washed repeatedly until neutral pH and filtered using PTFE filter paper. The acid treated MWCNT molecules were characterised using FTIR spectroscopy and FESEM images were analysed to study their morphology. Fig.1 gives a schematic representation of the functionalisation process [19].

2.3. Composite Preparation

Calcined HAp powder was used for composite fabrication. It was mixed with appropriate quantity of MWCNT (both functionalised and non functionalised) in a high energy planetary ball mill (Fritsche Pulverissette 5, Germany) at 300 rpm for 5 h , in acetone medium. The milled powders were sieved and used to prepare pellet samples (12 mm dia. × 4 mm thick) in a uniaxial press (PEECO, India) at 150 MPa for 2 min . Sintering was performed under argon atmosphere, in two steps: first upto 700 °C using a heating rate of 3 °C/min. and then upto 1250 °C at a heating rate of 6 °C/ min. (1 h dwel time). Detailed fabrication process of the composite has been discussed elsewhere [18]. Muller et al in their animal study indicated that MWCNT showed inflammation, granulomas, and fibrosis of lungs and also the unground CNTs remained in the bronchial lumen and produced collagen-rich granulomas [20]. Taking this into consideration, two different MWCNT loadings of 1% and 2% were studied for each of non functionalised and functionalised types , which were named as HC_1, HC_2, and HFC_1, HFC_2 respectively.

2.4. Characterization

X-ray diffraction (XRD, Ultima III Rigaku diffractometer, with CuK_α and a wave length of 0.154 nm) and Fourier transformed infrared spectroscopy (FTIR, IR-Prestige 21, 200VCE, Schimadzu, in mid IR region i.e., 4000-400 cm^{-1}) of the nanocomposites were carried out to study the formed phases. The microstructure and morphology were studied using a field emission scanning electron microscope (FESEM, Hitachi, S4800) and by high-resolution transmission electron microscopy (HRTEM, JEOL, JEM 2100). For TEM analysis, the sintered samples were ground to powders and dispersed in aqueous solutions by ultrasonication for 2 h. Dispersed solution was then added to carbon coated copper grids (300 mesh) and viewed. The bulk density (B.D.) and percent apparent porosity (A.P.) of the sintered samples were measured using Archimedes' water

displacement method, following ASTM standard (C373) and using the relationships, A.P.=[(W-D)/(W-S)]×100% and B.D.=[D/(W-S)] g/c.c.

where D, W and S are the dry weight, soaked weight and suspended weight of the samples respectively.

For any bioceramic material to be used for osseo-implant applications, the major challenge is to enhance the toughness without sacrificing its hardness and bioactivity [2]. In the present work, a series of macro and micro indentation studies were performed to analyse the aggregate mechanical behavior as well as to understand the effect of localized heterogeneity. The hardness (HV) and fracture toughness (K_{1C}) of the sintered samples (< 0.02 μm R_a) were evaluated using Vickers hardness tester (LECO, LV-700AT,) by indentation method (following ASTM C1327) with different indentation loads (0.3, 1, 3 and 5 kg_f with a holding time of 10 s each). HV was calculated from the method described in the ASTM E384 with standard formula for force divided by contact area [$HV=1.844\times(P/d^2)$], where HV is Vickers' hardness, P is the applied indenter load, and d is the average diagonal length for an individual indentation. From the indentation crack-length data K_{1C} was calculated by using the relation: $K_{1C}=\delta(E/H)^{0.5}\times(P/c^{1.5})$, where E is the Young's modulus, H is the hardness and δ is a constant that depends on the geometry of the indenter (0.016 ± 0.004 for standard Vickers diamond pyramid indenter).

Nanoindentation tests, which is an effective technique to evaluate the micromechanical properties of composites, was carried out in a Vickers Nanoindentor (H100, Fischer), at three different loads (10, 100 and 1000 mN). A maximum indentation depth of 100 nm was allowed with a dwell time of 10 s for each indentation. A minimum distance of 200-300 μm was maintained between adjacent indentations to avoid any stress-strain influence caused by the adjacent indentations. Loading and unloading curves were recorded using the in-built data acquisition software. The micro hardness and elastic modulus were calculated on the basis of the standard procedure using the Oliver and Pharr method [21].

Flexural and compressive strength of the nanocomposites were measured in a universal-testing machine (Instron 4204). The flexural strength (σ_f) was measured by three point-bending tests with rectangular specimens of dimension 60 mm ×10 mm × 6 mm using a crosshead speed of 0.50 mm/min., respectively, using the equation: $\sigma_f= (3Fl)/(2bd^2)$, where F is the load at the fracture point, l is the span length, b is the breadth and d is the thickness of the samples. Each

measurement was repeated and the average value was calculated. The fractographs were analysed using the FESEM technique. For compressive strength measurements, cylindrical samples with a length: diameter of 2:1 was used. The falling weight test was performed to evaluate the impact resistance of the nano biocomposites (slightly modifying the ASTM D5628). The sample was kept on two supports and the impact was applied on the sample from a fixed measured height using spherical strikers with mass varying between 0.5-5 g and diameter of 5-8 mm. The strikers were allowed to hit the samples at the centre at a constant striking rate and the impact resistance was calculated from the energy required to break the samples.

Cytoxicity of any biomaterial is evaluated by studying their percent haemolysis in blood. Cytotoxic materials rupture the RBC membranes and release the haemoglobin. Spectrometric analysis of the free haemoglobin helps to measure the extent of cytotoxicity (ASTM F756). Pretreated goat blood (mixed with anti-coagulant Na-citrate) was diluted with n-saline and incubated at 37 °C to provide thermal equilibrium. 0.2 mL of the diluted blood was added to the sample test tubes, mixed gently and incubated for another 1 h. To the positive control, Na_2CO_3 solution (Na_2CO_3 causes large scale rupture of RBC) was added, while n-saline (n-saline does not rupture RBC) was added to the negative control. After an incubation of 30 mins, all the samples including the control were centrifuged. OD of the supernatant was measured at 545 nm using the UV-VIS spectroscope (Perkin Elmer, Lambda 35). Detail of the procedure has been discussed elsewhere [20]. The percentage haemolysis was calculated using the equation: $\text{Haemolysis (\%)}=[(OD)_{test}-(OD)_{Negative}]/[(OD)_{Positive}-(OD)_{Negative}]$.

3. Results and discussions

3.1. Functionalisation of carbon nanotubes

FTIR spectra of CNT chains, both pristine and functionalised, are shown in Fig. 2a and 2b respectively. FTIR of pristine CNT exhibits a single peak at 2359 cm^{-1}, corresponding to the C=C stretching [22] while the acid treated CNT (Fig. 2B) gives characteristic peaks at 1053, 1226, 1718, 2854, 2926, 3375 and 3722 cm^{-1} [23]. The broad band around 3375 and 3722 cm^{-1} is attributed to the presence of water and hydroxyl functional groups (ν_{OH}) that may have resulted

from the carboxylation process. The peak at 2926 cm^{-1} corresponds to stretching of C-H bonds while that around 1718 and 1053 cm^{-1} can be attributed to the stretching of carbonyl ($\nu_{C=O}$) and ester (ν_{C-O}) bonds, respectively. The peaks at 1226, 1396 and 2304 cm^{-1} corresponds to the C=C stretching. All these peaks are indicative of the carboxylation of the MWCNT surface through the acid treatment process [23].

Figs. 3a and3b show the optical images of aqueous suspensions of pristine and acid treated MWCNTs which further confirms the functionalisation procedure. The figure exhibits that the suspension of the pristine CNT which remain in agglomerations due to strong inter-chain van der Waals attraction, are not stable and the chains settle down at the bottom, giving two distinctly separate layers (Fig. 3a). On the other hand, the acid-treated CNT molecules form a successful dispersion and no precipitation was observed even after 24 h (Fig. 3b). This may be attributed to the lowering of the inter chain interactions because of surface treatment of the CNTs. The observation was also manifested in the FESEM images, shown in Figs. 4a and 4b respectively. The micrographs clearly exhibit the thickening of the chains of the acid treated nanotubes in comparison to the unreacted ones. It is seen that while the chain diameters of the pristine nanotubes vary between 20-50 nm, that of the acid treated ones vary between 40-80 nm. Also there is a substantial decrease in the chain length of the molecules. These are primarily due to acid treatment of the pristine chains resulting in functionalisation of their sidewalls (Fig. 1).

3.2. XRD and FTIR analysis

XRD analysis of the HAp-CNT composites as well as that of pristine and functionalised CNTs are shown in Fig. 5a and 5b respectively. It is observed that the main phase of the composites is pure HAp (matches with JCPDS PDF #09-0432), with three most intense peaks corresponded to (211), (300) and (002) planes respectively. Absence of any new peak confirms that no new compound was formed due to the addition of CNT in the ceramic matrix. The main graphitic peak (002) of CNTs ($2\theta = 26.6°$) (JCPDS PDF #41-1487) [24] was not observed in the diffraction patterns of the composites. This is mainly because the small amount of the CNT used for the composite preparation was difficult to detect within the sensitivity limit of the instrument.

The formation of HAp-CNT nanocomposites were further confirmed by analyzing the FTIR spectra (Fig. 6). Pure HAp exhibited characteristic peaks at 563.2, 601.8, 962.4, 1033.84, 1095.6, 1413.8, 1649.1 and 3444.8 cm^{-1} (Fig. 6), which agrees with the literature [25]. The bands at

563.2, 601.8, 962.4 and 1033.84 cm^{-1} are attributed to the stretching modes of phosphate group of HAp [25, 26] while the hydroxyl group gives characteristic peaks at 1649.1 and 3444.8 cm^{-1}. The figure shows that the composites, both with non-functionalised as well as functionalised CNTs, possess peaks similar to pure HAp, except for the hydroxyl group (-OH) which is absent for the composites. This is due to the loss of the extra moisture during the sintering procedure. The peaks of HC_1 and HC_2 are similar to that of pure HAp while HFC_1 and HFC_2 possessed added peaks at 1459.8 and 1539.3 cm^{-1} , which may be attributed to carbonate groups [25]. The similar nature of the FTIR patterns of the composites to that of pure HAp leads to the conclusion that presence of CNT in the HAp-CNT composites does not alter the basic structure of the monophasic HAp.

3.3. Physical properties

Fig. 7 shows the changes in A.P. and B.D. as function of CNT content. The figure shows that there is decrease in bulk density with increase in CNT loading, the density being minimum at 2% loading. Also, the porosity is maximum for the 2% composite. This may be due to the very low density of the CNT powders as compared to bulk HAp. However, the overlapping error bars suggest that the difference in bulk density is not very high and lies within the experimental scatter.

3.4. Microstructure

The FESEM morphology of HAp-CNT composites are shown in Fig. 8a-c. This exhibit porous nature of the nanocomposites which very favorable for cellular growth with presence of fine hair like CNT chains attached to the HAp grains. Fig. 8a reveals the agglomerated pristine CNT chains, embedded in the HAp matrix while Fig. 8b shows that the functionalised CNT chains are distributed in the ceramic matrix. However fractured micrographs of the nanocomposites (Fig. 8c) show the bridging action of the CNT chains, across the cracks moving along the grain boundaries, which confirm the crack-resisting mechanism of the nanocomposites [18] .This bridging action of the nanotubes is observed with both types of composites. The HRTEM images of the sintered composites (Figs. 9a-d) exhibited HAp particles adhered to nanotubes with good uniformity. MWCNT hollow chains were evident with HAp particles closely associated with

little or no interfacial gap. Closed pores in the sintered HAp crystals were also seen. This is again confirmed from lattice fringes of sintered composites (Fig. 10) where it is seen that the lattices of CNT chains and HAp remained mixed together. Different lattice spacing of HAp and MWCNT (interlayer distance between the walls) have also been shown in which 0.312 nm represented MWCNT [2].

3.5. Mechanical properties

HV (in GPa) and K_{1c} of the composite samples are shown in Figs. 11a and 11b. It is observed that Vickers hardness of the composites reinforced with functionalised CNT chains is marginally higher than those fabricated using pristine CNT molecules.

In order to investigate the micromechanical properties, namely hardness and elasticity, nanoindentation tests of the nanocomposites with different CNT loadings were performed. Fig. 12 a-c represent the load-indentation depth curves of the HAp-CNT nanocomposites, both with pristine (HC_1, HC_2) and functionalised CNTs (HFC_1, HFC_2). The plots show that the nature of the load-indentation depth plots of HAp-CNT composite is same for all the loads (10, 100 and 1000 mN) with 2% pristine CNT giving the minimum value of both hardness and Young's modulus. Also, HFC_1 and HFC_2 appear to possess improved hardness and elastic modulus.

Fig.13 shows the percentage increase of flexural strength of the composites over that of pure HAp. It is found that while HC_1, HFC_1 and HFC_2 exhibited an increase of 120-144 % over pure HAp, HC_2 exhibited almost 350% increase. This manifold improvement in flexural strength with the addition 2% CNTs may be attributed to the superior tensile properties of the CNT molecules being imparted to the nanocomposite.

Impact resistance has been done thoroughly with the help of drop weight test configuration with the different sized hardened steel ball (ensuring point contact during impact) impacting the specimen kept in simply supported situation. At least three samples were broken from each composition wherefrom an average data has been reported here. The results are mentioned in the

Table 1. It clearly revealed that composite specimens showed better impact resistance than pure HAp. This superiority of the nanocomposites may be attributed to the crack bridging action of the CNT as pointed out in the discussion of fracture toughness. Regarding the stress intensity factor, K_{1c} values already reported in the paper (Fig. 11b) reveals the critical stress intensity factor values for the specimens using indentation technique. The tests were done with various loads which resulted in variation in indentation crack lengths and there from an average value has been reported. The scatter in critical stress intensity factor as a function of indentation load was quite low, no systematic pattern of variation of stress intensity factor with load was noticed.

3.6. Haemocompatibility study

The results of the haemocompatibility experiments are given in Table 2. As per the ASTM standard (ASTM F756), any material with a percent haemolysis of less than 10, is considered as haemocompatible, and if the value is less than 5, it is highly haemocompatible. Table 1 shows that the HAp-CNT composites, fabricated with both pristine as well as carboxylated MWCNTs, exhibit a haemocompatibility between 0.3-3.9%. Thus it can be inferred that the nanocomposites are highly haemocompatible. It can also be concluded that the haemocompatibility of the monophasic HAp ceramics is not affected by the incorporation of CNT molecules and functionalisation.

4. Conclusions

In the present work, pristine MWCNT chains were functionalised with carboxyl groups using strong acid mixture (3:1 H_2SO_4:HNO_3). Sintered nanocomposites of monophasic HAp were prepared using both pristine as well as functionalised MWCNT chains. A comparative study of their physical, mechanical and biocompatibility were done. XRD and FTIR analysis showed that the main phase of all the composites were HAp. FTIR showed that the composites with the functionalised CNT chains exhibited added peaks due to the presence of C=O groups resulting due to the carboxylation. The composites possessed good density with considerable porosity, favorable for tissue growth. Bridging action of the CNT chains across the advancing cracks could be observed with both types of composites. It helped to retard the propagation of the crack. Nano hardness and elasticity of HFC_1 and HFC_2 was found to be higher than that of HC_1 and HC_2, but the values were within the experimental scatter. High experimental scatter may be

attributed to the presence of local level heterogeneity in the composites. Microstructural analysis revealed that while the non functionalised CNT chains were present in agglomerated states around the HAp grains, the acid treated chains were relatively more dispersed, although some amount of agglomeration still existed. So the advantage of functionalisation could not be exploited fully. Further optimisation in functionalisation process is required to ensure better dispersion of CNT.

Acknowledgements

The authors would like to thank Dr. P.K. Das, Chief Scientist, Non-Oxide Ceramics Division, CSIR-CGCRI for his help during sample preparations. Help and support rendered by Mr. A. Pradhan, Department of Chemical Engineering and Mr. P.C. Pramanik, School of Bioscience and Engineering of Jadavpur University, are sincerely acknowledged. One of the authors (SM) wishes to thank would like to acknowledge the University Grants Commission (UGC) for financial support and Council of Scientific and Industrial Research (CSIR) for providing fellowship .

References

[1] L.L. Hench, Bioceramics: From concept to clinic, Journal of the American Ceramic Society 74 (7) (1991) 1487-1510.
[2] A.A. White, S.M. Best, I.A. Kinloch, Hydroxyapatite-carbon nanotube composites for biomedical applications: A review, International Journal of Applied Ceramic Technology 4 (1) (2007) 1-13.
[3] J. Chen, W. Tong, Y. Cao, J. Feng, X. Zhang, Effect of atmosphere on phase transformation in plasma-sprayed hydroxyapatite coatings during heat treatment, Journal of Biomedical Materials Research 34 (1) (1997) 15-20.
[4] C. Balcik, T. Tokdemir, A. Senkoylu, N. Koc, M. Timucin, S. Akin, P. Korkusuz, F. Korkusuz, Early weight bearing of porous HA/TCP (60/40) ceramics in vivo: A longitudinal study in a segmental bone defect model of rabbit, Acta Biomaterialia 3 (6) (2007) 985-996.
[5] Y. Zhang, S. Tan, Y. Yin, C-fibre reinforced hydroxyapatite bioceramics, Ceramics International 29 (1) (2003) 113-116.
[6] X. Zhang, G.M. Gubbels, R.A. Terpstra, R. Metselaar, Toughening of calcium hydroxyapatite with silver particles, Journal of Materials Science 32 (1) (1997) 235-243.
[7] J. Li, H. Liao, L. Hermansson, Sintering of partially-stabilised zirconia and partially-stabilised zirconia-hydroxyapatite composites by hot isostatic pressing and pressureless sintering, Biomaterials 17 (18) (1996) 1787-1790.

[8] J. Li, B. Fartash, L. Hermansson, Hydroxyapatite-alumina composites and bone-bonding, Biomaterials 16 (5) (1995) 417-422.
[9] S. Iijima, Helical microtubules of graphitic carbon, Nature 354 (6348) (1991) 56-58.
[10] M.S. Dresselhaus, G. Dresselhaus, A. Jorio, Unusual properties and structure of carbon nanotubes, Annu. Rev. Mater. Res. 34 (2004) 247-278.
[11] M.-F. Yu, O. Lourie, M.J. Dyer, K. Moloni, T.F. Kelly, R.S. Ruoff, Strength and breaking mechanism of multiwalled carbon nanotubes under tensile load, Science 287 (5453) (2000) 637-640.
[12] R.S. Ruoff, D.C. Lorents, Mechanical and thermal properties of carbon nanotubes, Carbon 33 (7) (1995) 925-930.
[13] A. Hirsch, Functionalisation of single-walled carbon nanotubes, Angewandte Chemie International Edition 41 (11) (2002) 1853-1859.
[14] A. Eitan, K. Jiang, D. Dukes, R. Andrews, L.S. Schadler, Surface modification of multiwalled carbon nanotubes: toward the tailoring of the interface in polymer composites, Chemistry of Materials 15 (16) (2003) 3198-3201.
[15] T. Lei, L. Wang, C. Ouyang, N.F. Li, L.S. Zhou, In situ preparation and enhanced mechanical properties of carbon nanotube/hydroxyapatite composites, International Journal of Applied Ceramic Technology 8 (3) (2011) 532-539.
[16] Y.-P. Sun, K. Fu, Y. Lin, W. Huang, Functionalised carbon nanotubes: Properties and applications, Accounts of Chemical Research 35 (12) (2002) 1096-1104.
[17] B. Kundu, M.K. Sinha, M.K. Mitra, D. Basu, Fabrication and characterization of porous hydroxyapatite ocular implant followed by an in vivo study in dogs, Bulletin of Materials Science 27 (2) (2004) 133-140.
[18] S. Mukherjee, B. Kundu, S. Sen, A. Chanda, Improved properties of hydroxyapatite-carbon nanotube biocomposite: Mechanical, in vitro bioactivity and biological studies, Ceramics International 40 (4) (2014) 5635-5643.
[19] A.A. White, I.A. Kinloch, A.H. Windle, S.M. Best, Optimization of the sintering atmosphere for high-density hydroxyapatite-carbon nanotube composites, Journal of the Royal Society Interface 7 (Suppl 5) (2010) S529-S539.
[20] J. Muller, F. Huaux, N. Moreau, P. Misson, J.-F. Heilier, M. Delos, M. Arras, A. Fonseca, J.B. Nagy, D. Lison, Respiratory toxicity of multi-wall carbon nanotubes, Toxicology and Applied Pharmacology 207 (3) (2005) 221-231.
[21] W.C. Oliver, G.M. Pharr, An improved technique for determining hardness and elastic modulus using load and displacement sensing indentation experiments, Journal of Materials Research 7 (6) (1992) 1564-1583.
[22] M. Krishna Kumar, A. Leela Mohana Reddy, S. Ramaprabhu, Exfoliated single-walled carbon nanotube-based hydrogen sensor, Sensors and Actuators B: Chemical 130 (2) (2008) 653-660.
[23] D. Pan, Y. Wang, Z. Chen, T. Yin, W. Qin, Fabrication and characterization of carbon nanotube-hydroxyapatite nanocomposite: Application to anodic stripping voltammetric determination of cadmium, Electroanalysis 21 (8) (2009) 944-952.
[24] B.-D. Hahn, J.-M. Lee, D.-S. Park, J.-J. Choi, J. Ryu, W.-H. Yoon, B.-K. Lee, D.-S. Shin, H.-E. Kim, Mechanical and in vitro biological performances of hydroxyapatite-carbon nanotube composite coatings deposited on Ti by aerosol deposition, Acta Biomaterialia 5 (8) (2009) 3205-3214.

[25] I. Rehman, W. Bonfield, Characterization of hydroxyapatite and carbonated apatite by photo acoustic FTIR spectroscopy, Journal of Materials Science: Materials in Medicine 8 (1) (1997) 1-4.
[26] T.K. Anee, M. Ashok, M. Palanichamy, S. Narayana Kalkura, A novel technique to synthesize hydroxyapatite at low temperature, Materials Chemistry and Physics 80 (3) (2003) 725-730.

Legends of figures and tables

Table 1: Haemolysis (%) of HAp-CNT composite samples

Table 2: Impact resistance of HAp-CNT composite samples

Fig. 1: Schematic representation of the carboxylation of the MWCNT chains

Fig. 2: FTIR patterns of (a) pristine MWCNT and (b) acid treated MWCNT chains

Fig. 3: Aqueous dispersion of (a) pristine MWCNT and (b) acid treated MWCNT chains

Fig. 4: FESEM images showing (a) pristine MWCNT and (F) acid treated MWCNT

Fig. 5: XRD patterns of (a) HAp-CNT composite and (b) pristine and acid treated CNT chains

Fig. 6: FTIR patterns of different HAp-CNT composites

Fig. 7: Bulk density and apparent porosity of different HAp-CNT composites

Fig. 8: FESEM images of HAp-CNT composites showing (a) agglomerated chains of pristine MWCNT (marked with arrows), (b) uniformly distributed chains of functionalised MWCNT chains (marked with arrows) and (c) bridging action of CNT chains (marked with arrows) across the cracks in HAp matrix

Fig. 9: HRTEM images of the sintered HAp-CNT composites taken at different locations

Fig. 10: Lattice spacing calculated in the HAp-CNT sintered composite matrix

Fig. 11: Variations of HV and K_{1c} of different HAp-CNT composites

Fig. 12: Variations of nano-indentation (NI) H and E of different HAp-CNT composites under different loading conditions; 10 mN (a), 100 mN (b) and 1000 mN (c)

Fig. 13: % increase of flexural and compressive strength for different HAp-CNT composites over pure sintered HAp specimen

Table 1: Haemolysis (%) of HAp-CNT composite samples

Sample	% Haemolysis	Standard deviation
HAp	0.34	±0.03
HC_1	1.15	± 0.11
HC_2	1.75	± 0.13
HFC_1	3.34	±0.23
HFC_2	3.93	± 0.21

Table 2: Impact resistance of HAp-CNT composite samples

Sample	Impact energy, J/m^2	Standard deviation
HAp	47.25	2.68
HC_1	133.10	11.54
HC_2	122.95	7.16
HFC_1	78.26	2.02
HFC_2	144.96	22.12

Table 1: Haemolysis (%) of HAp-CNT composite samples

Sample	% Haemolysis	Standard deviation
HAp	0.34	±0.03
HC_1	1.15	± 0.11
HC_2	1.75	± 0.13
HFC_1	3.34	±0.23
HFC_2	3.93	± 0.21

Table 2: Impact resistance of HAp-CNT composite samples

Sample	Impact energy, J/m^2	Standard deviation
HAp	47.25	2.68
HC_1	133.10	11.54
HC_2	122.95	7.16
HFC_1	78.26	2.02
HFC_2	144.96	22.12

Figure 1

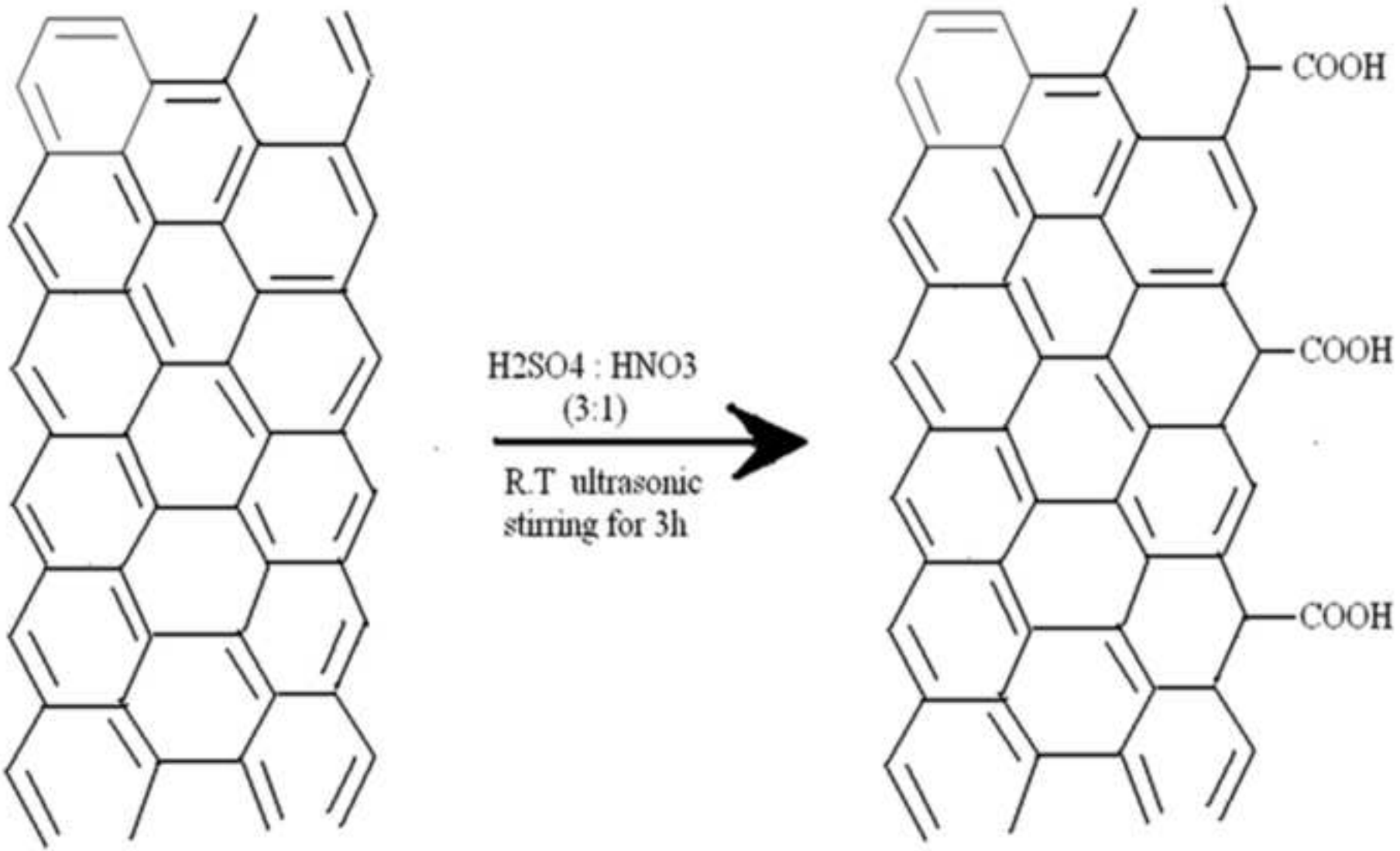

Figure 2a

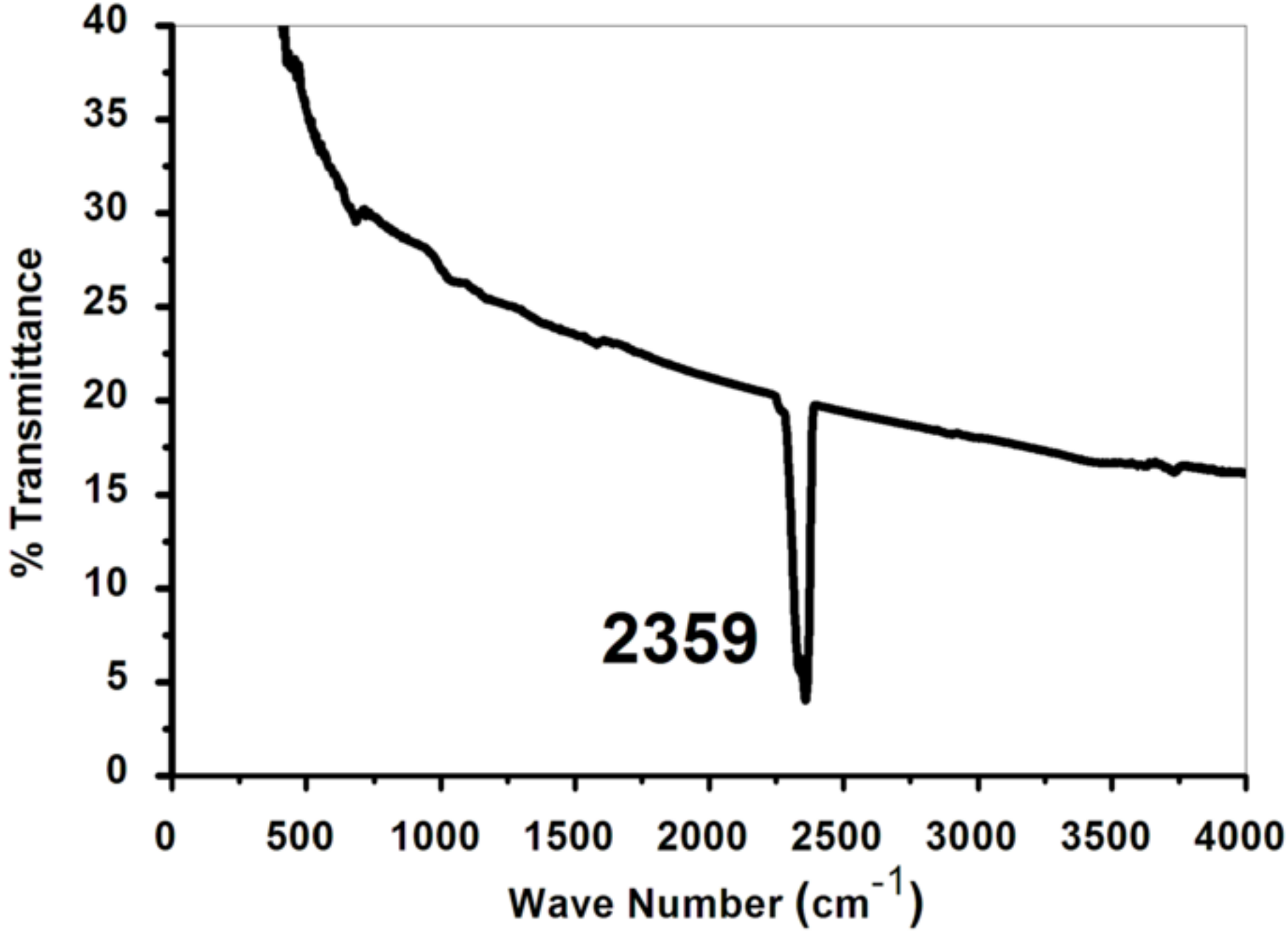

Figure 2b

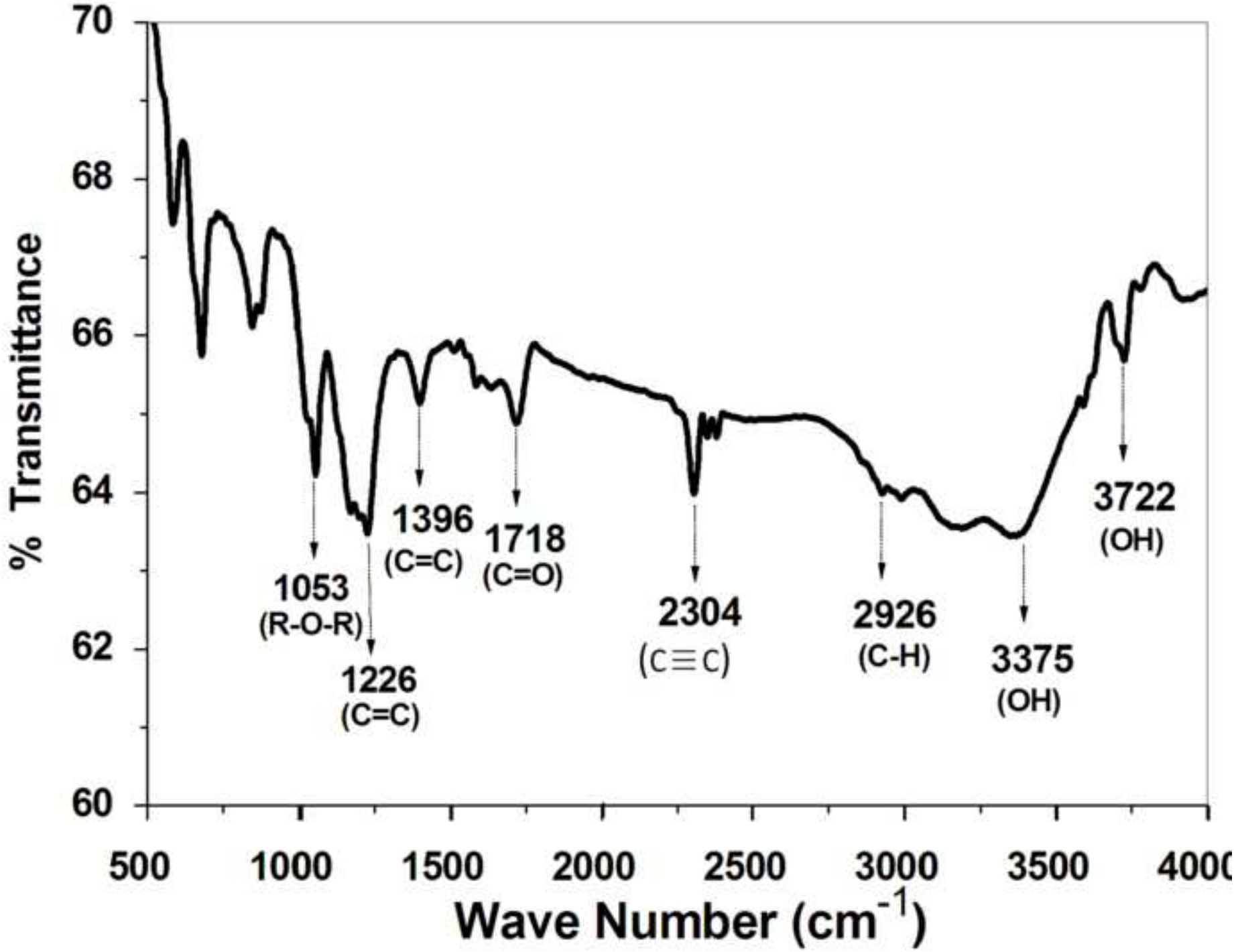

Figure 3

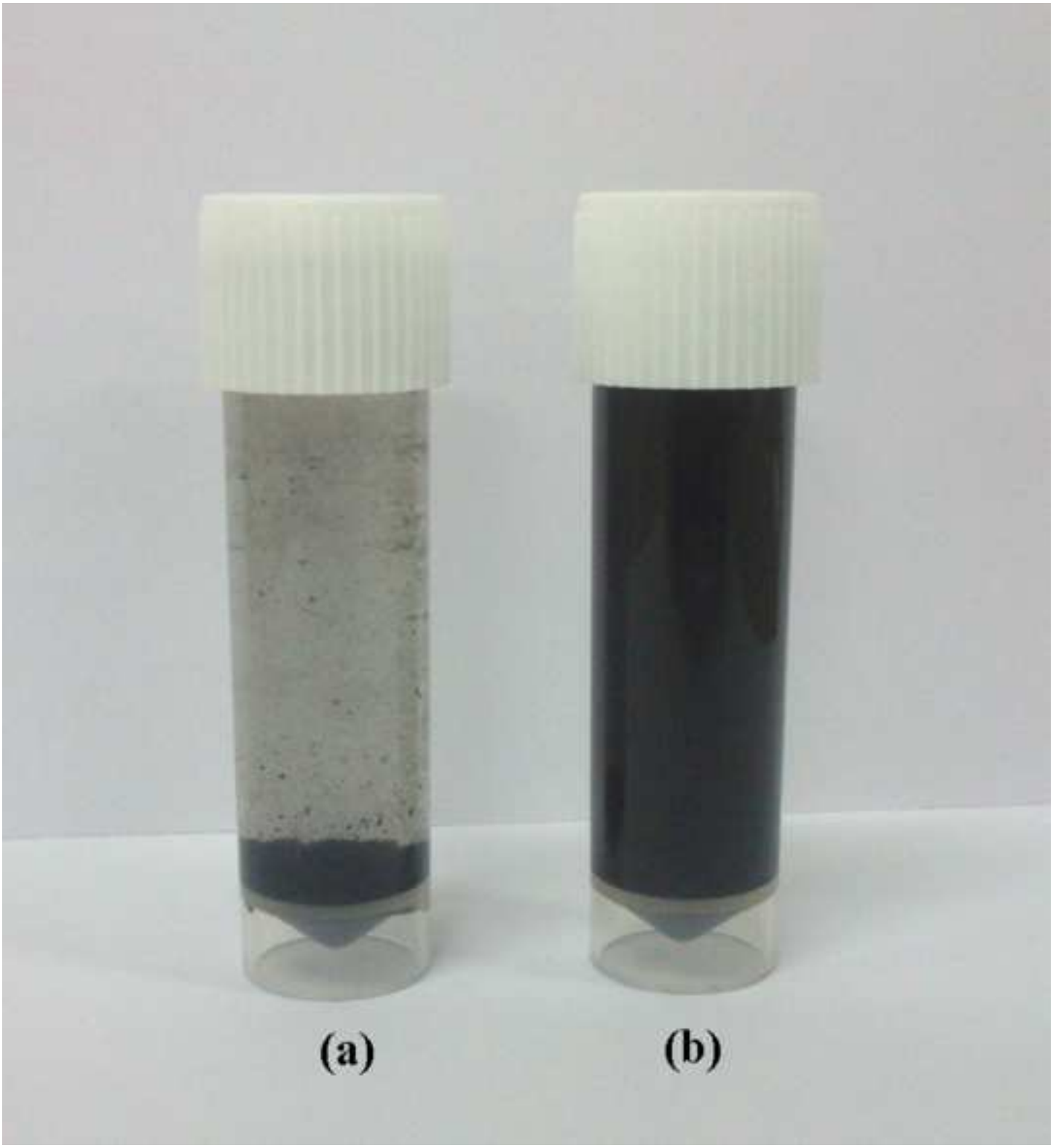

Figure 4a

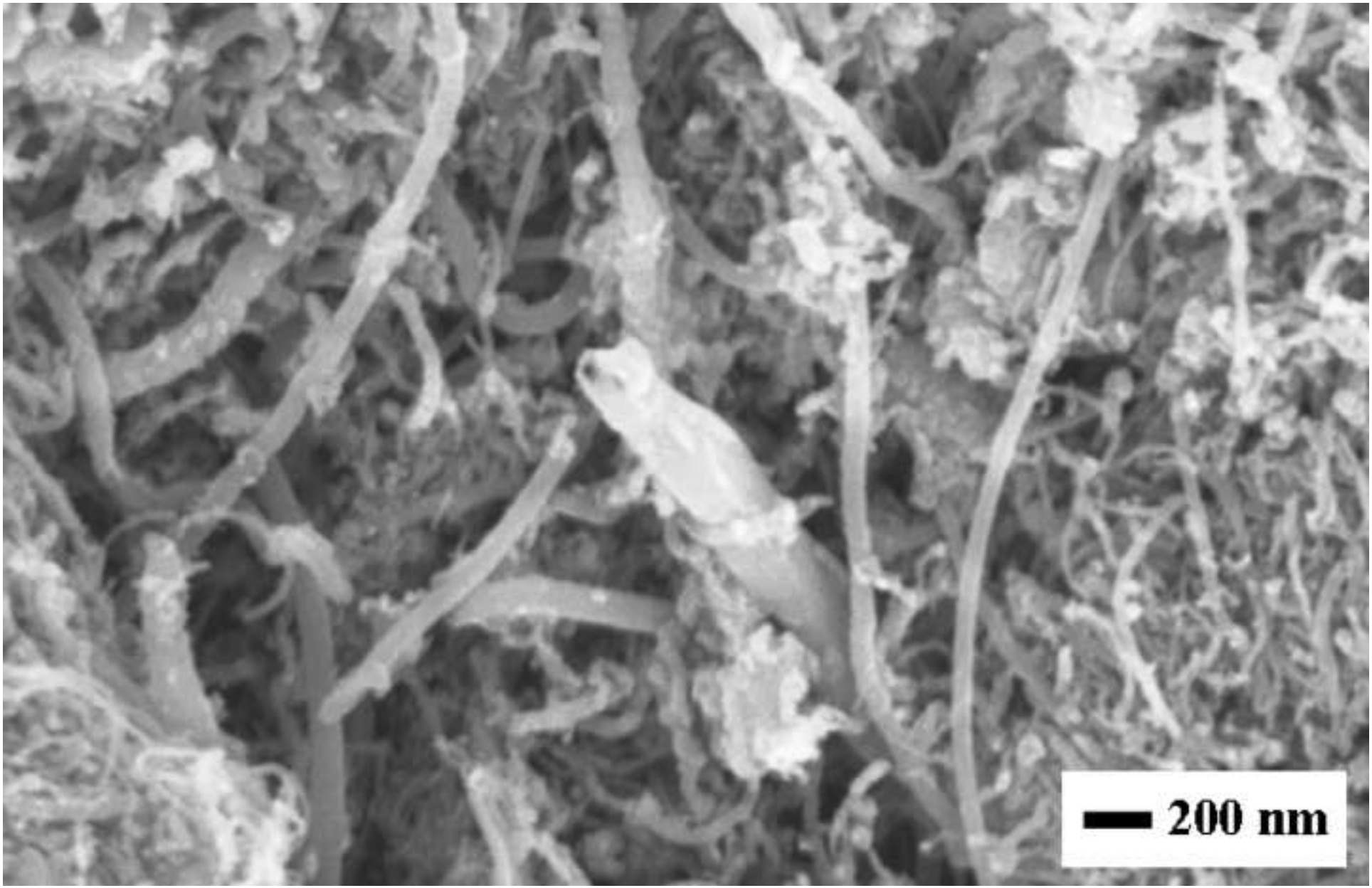

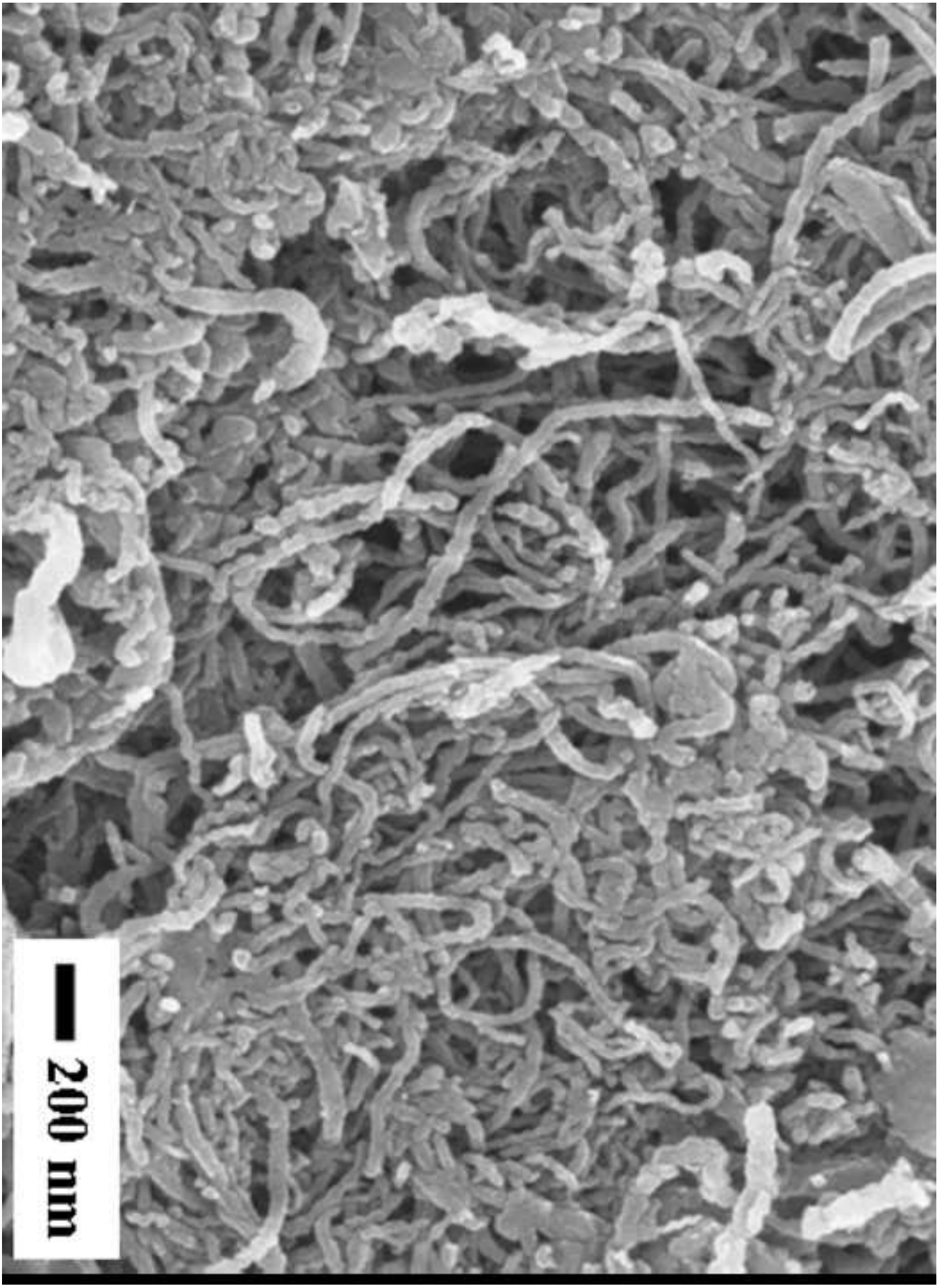

Figure 4b

Figure 5a

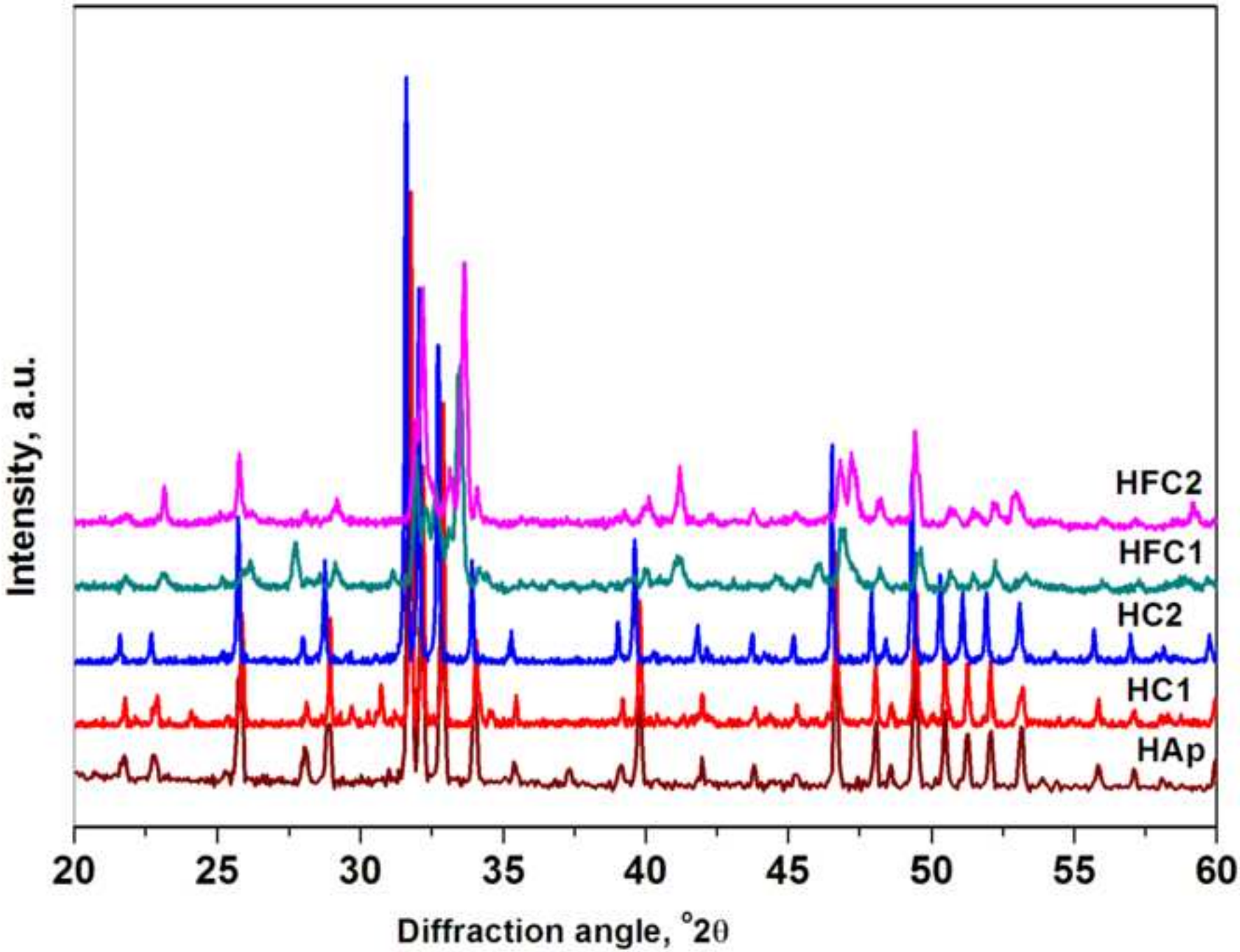

Figure 5b

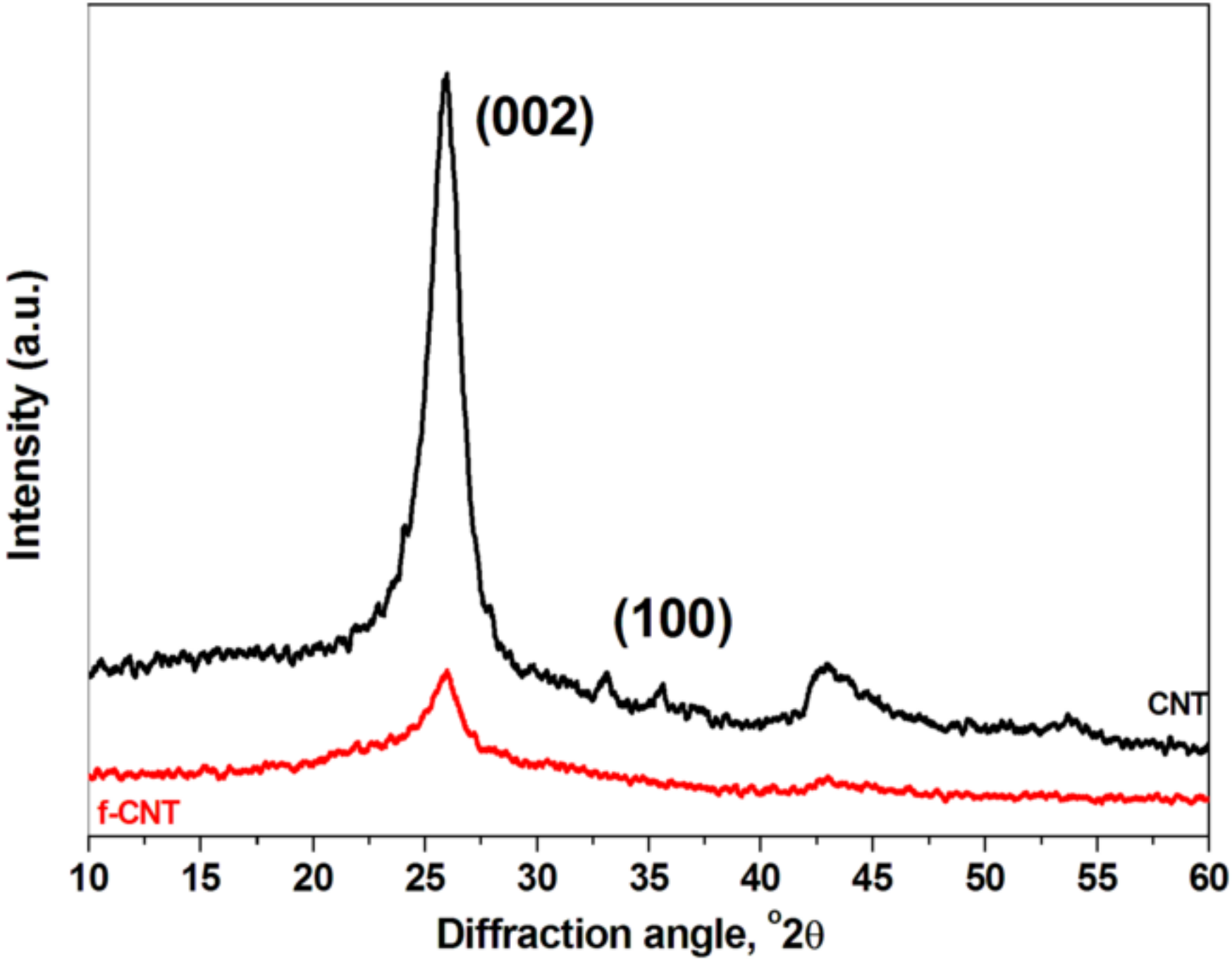

Figure 6

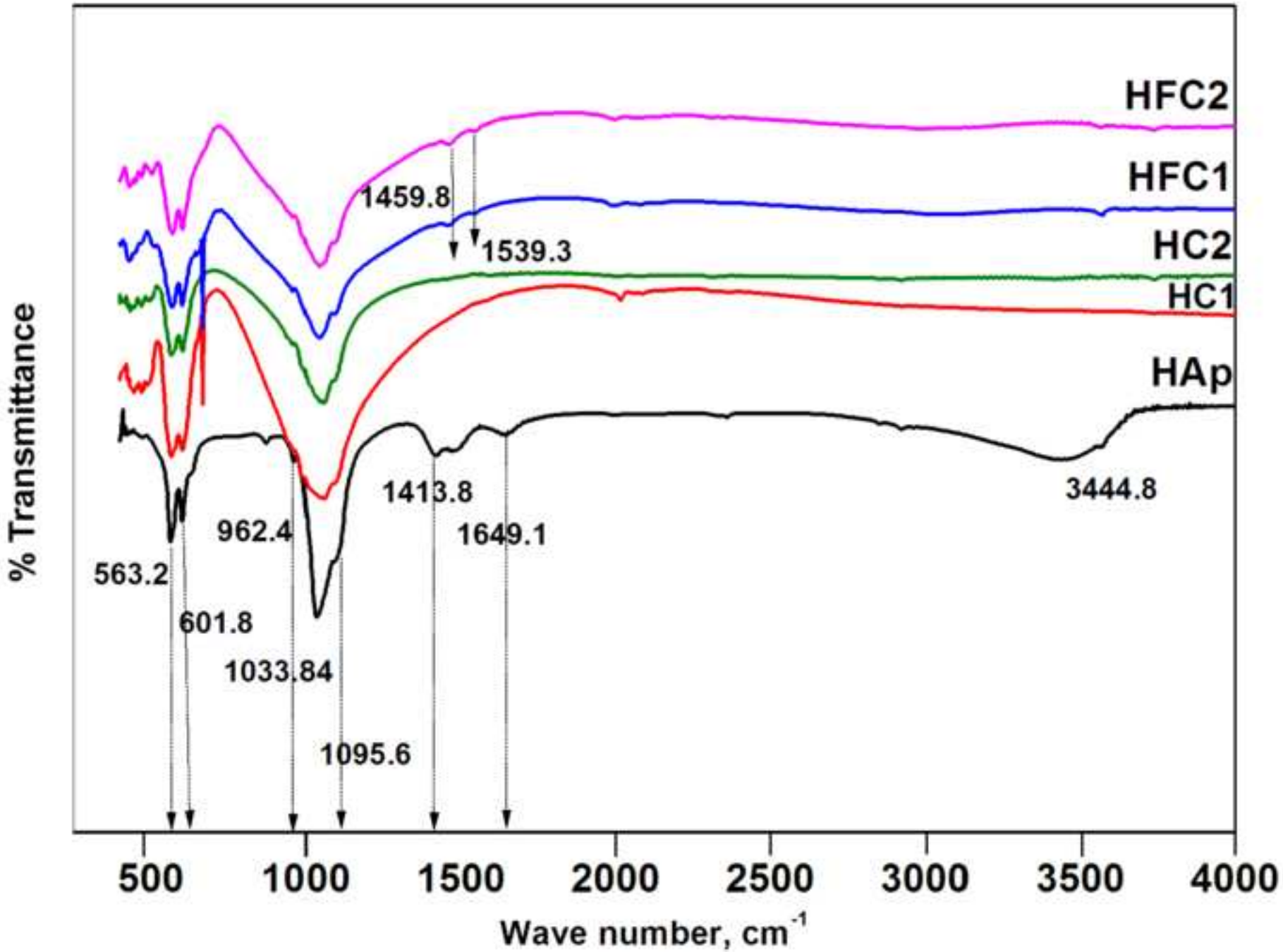

Figure 7

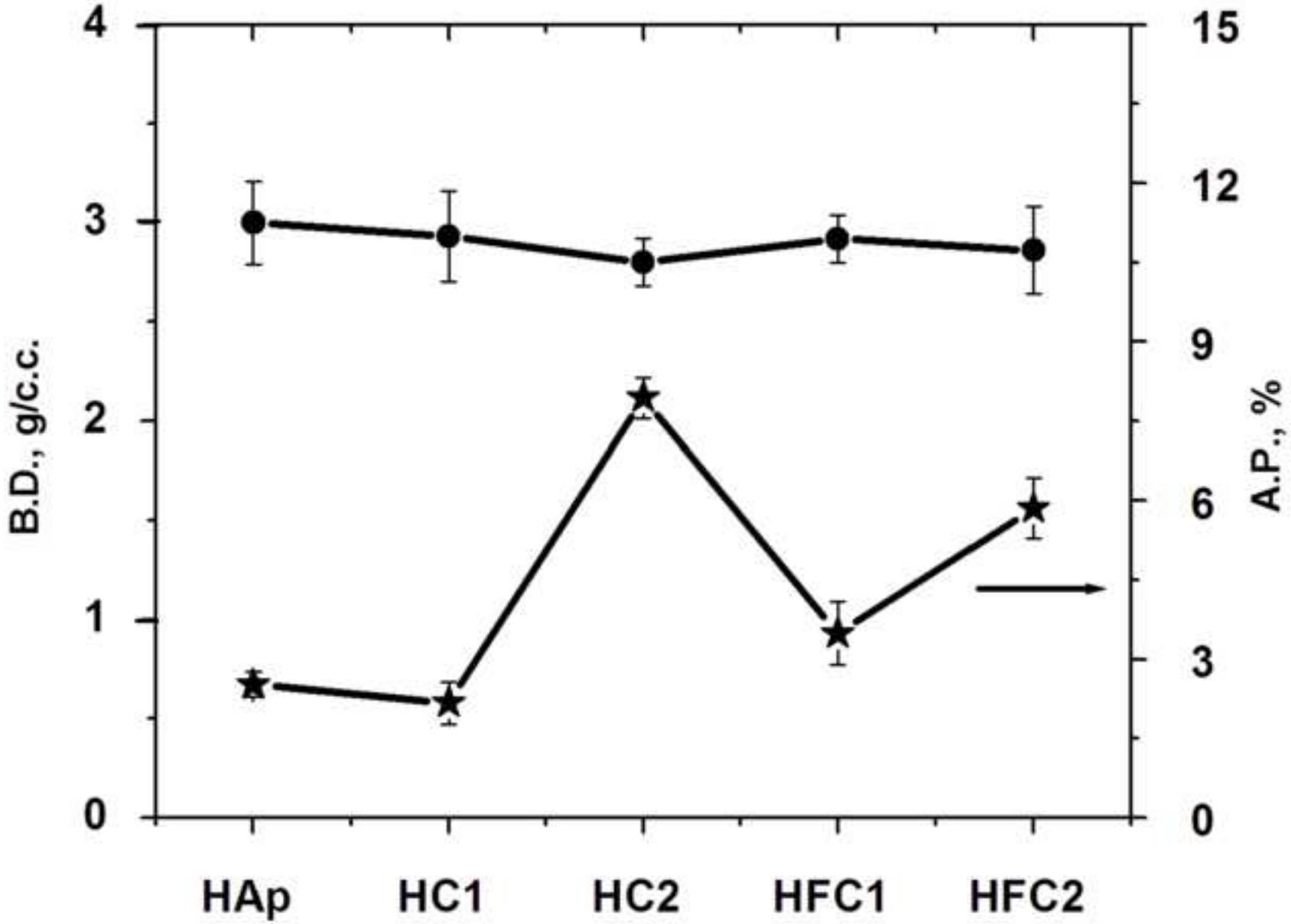

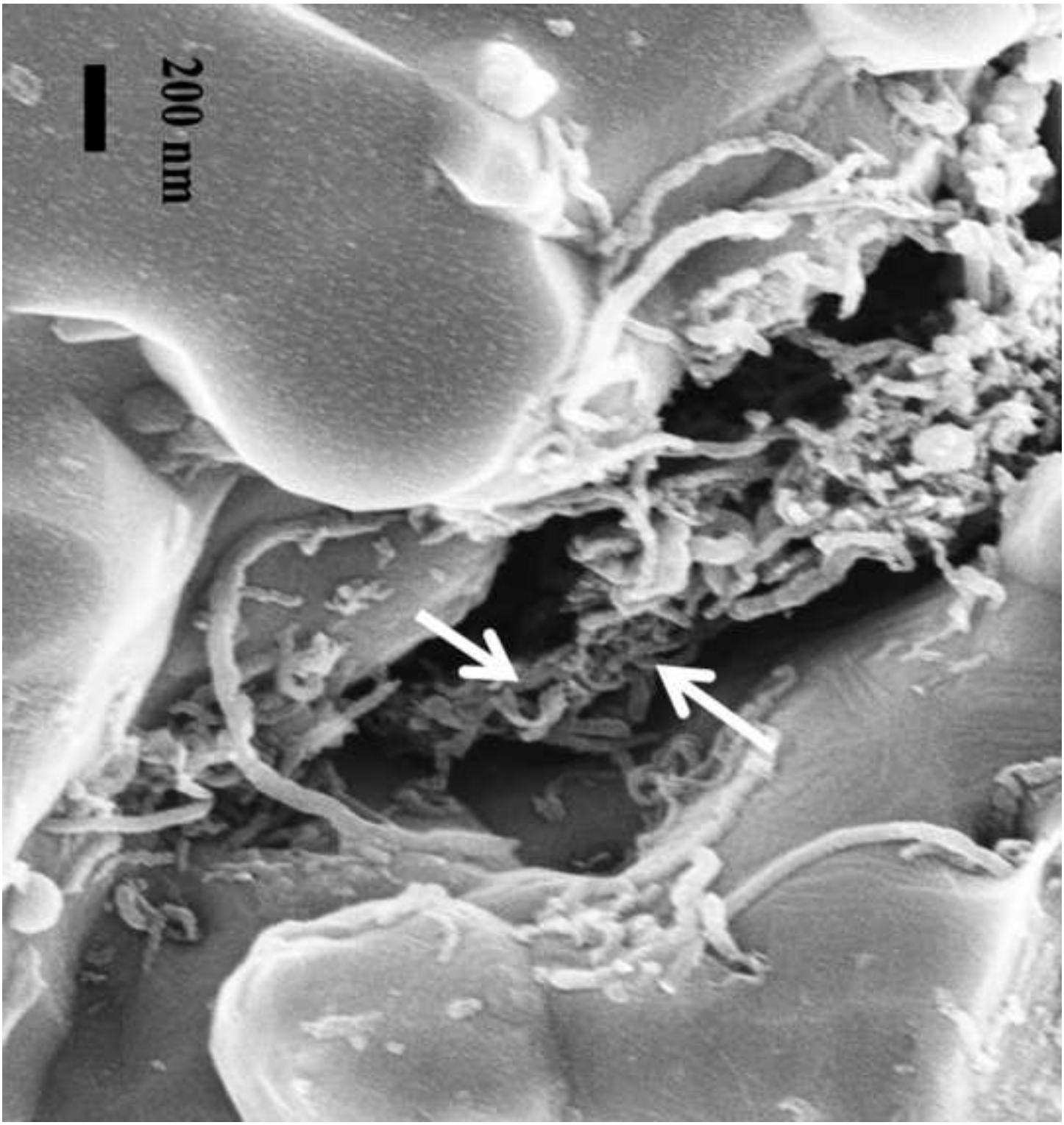

Figure 8a

Figure 8b

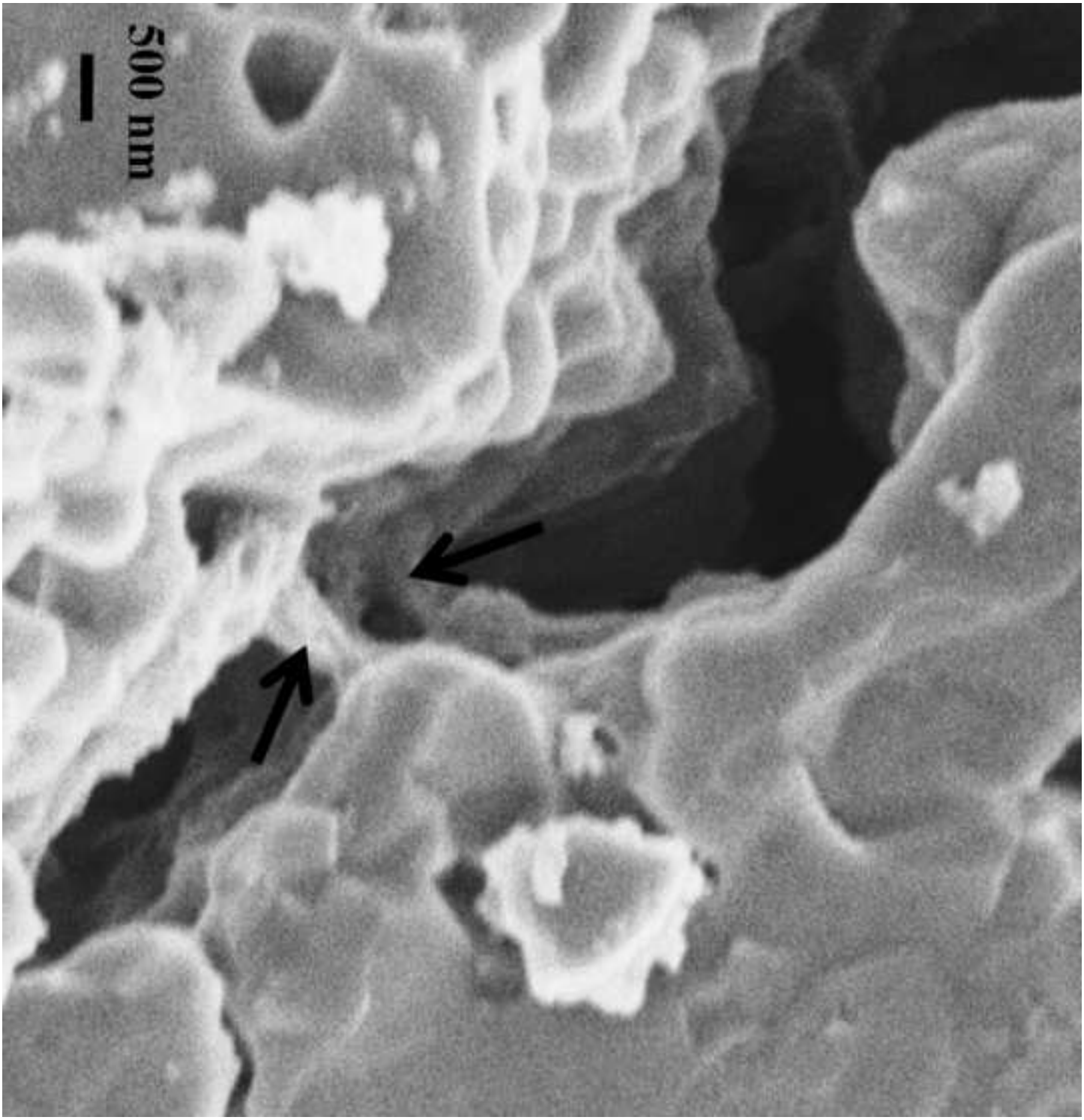

Figure 8c

Figure 9a

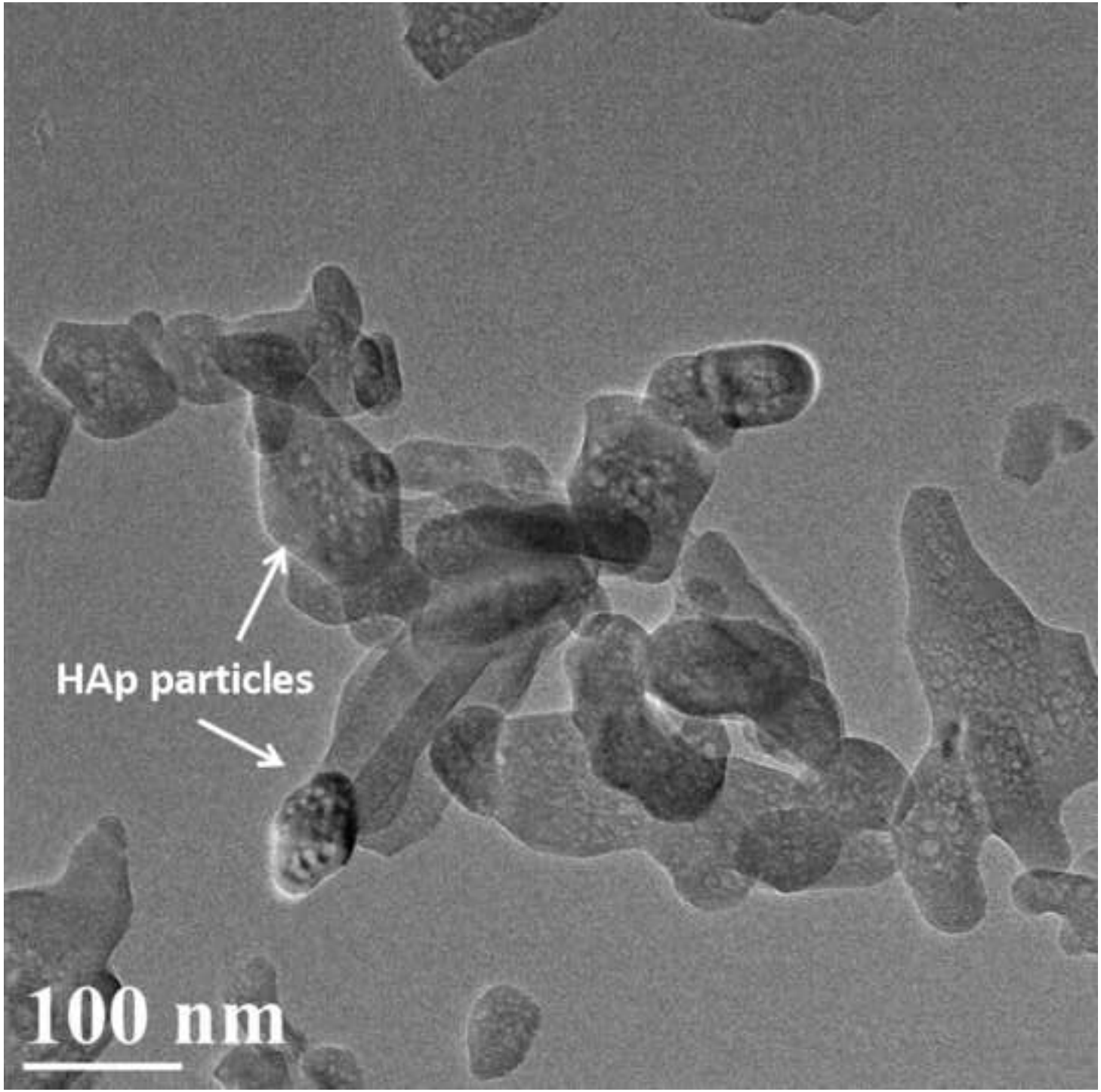

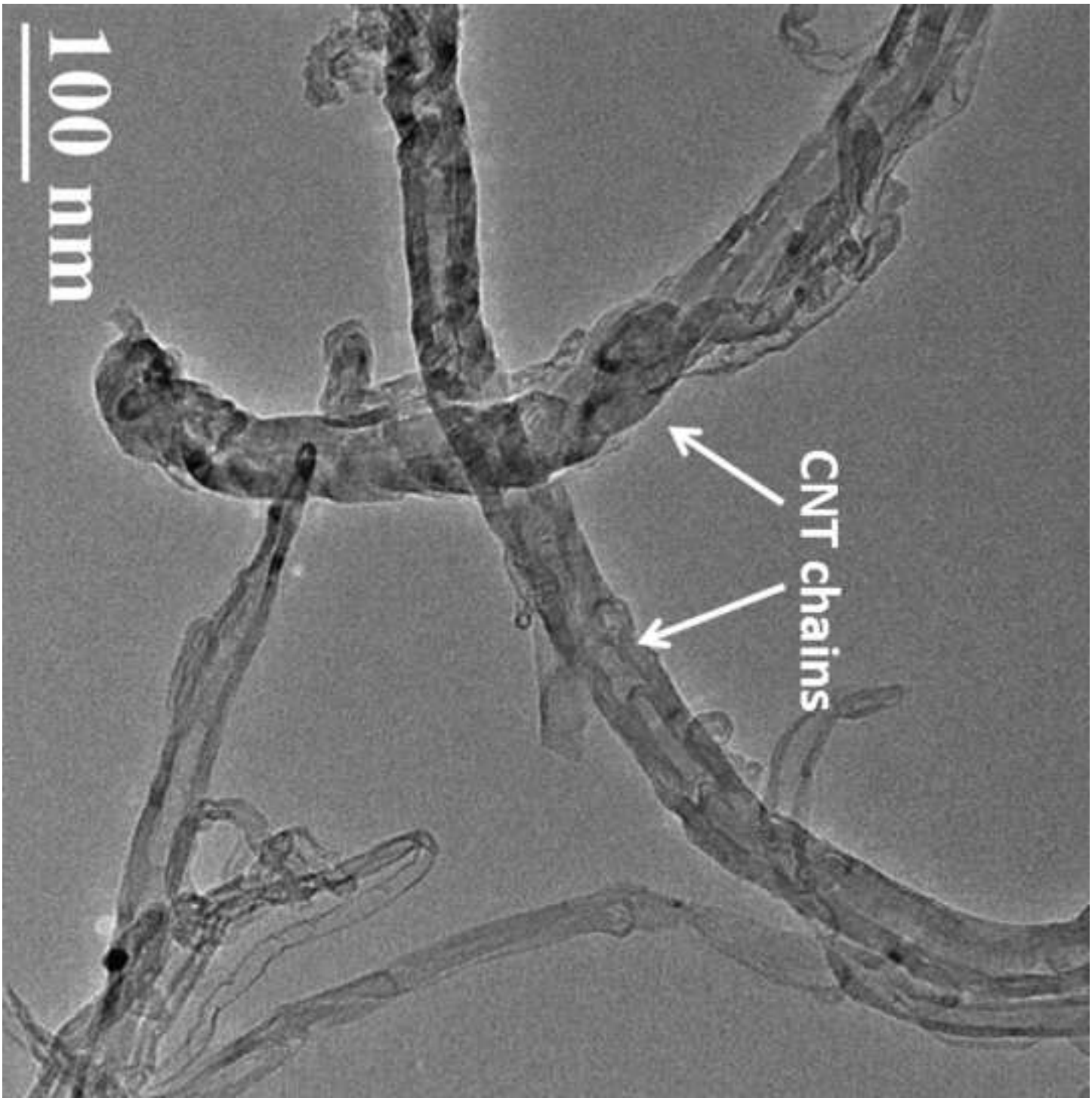

Figure 9b

Figure 9c

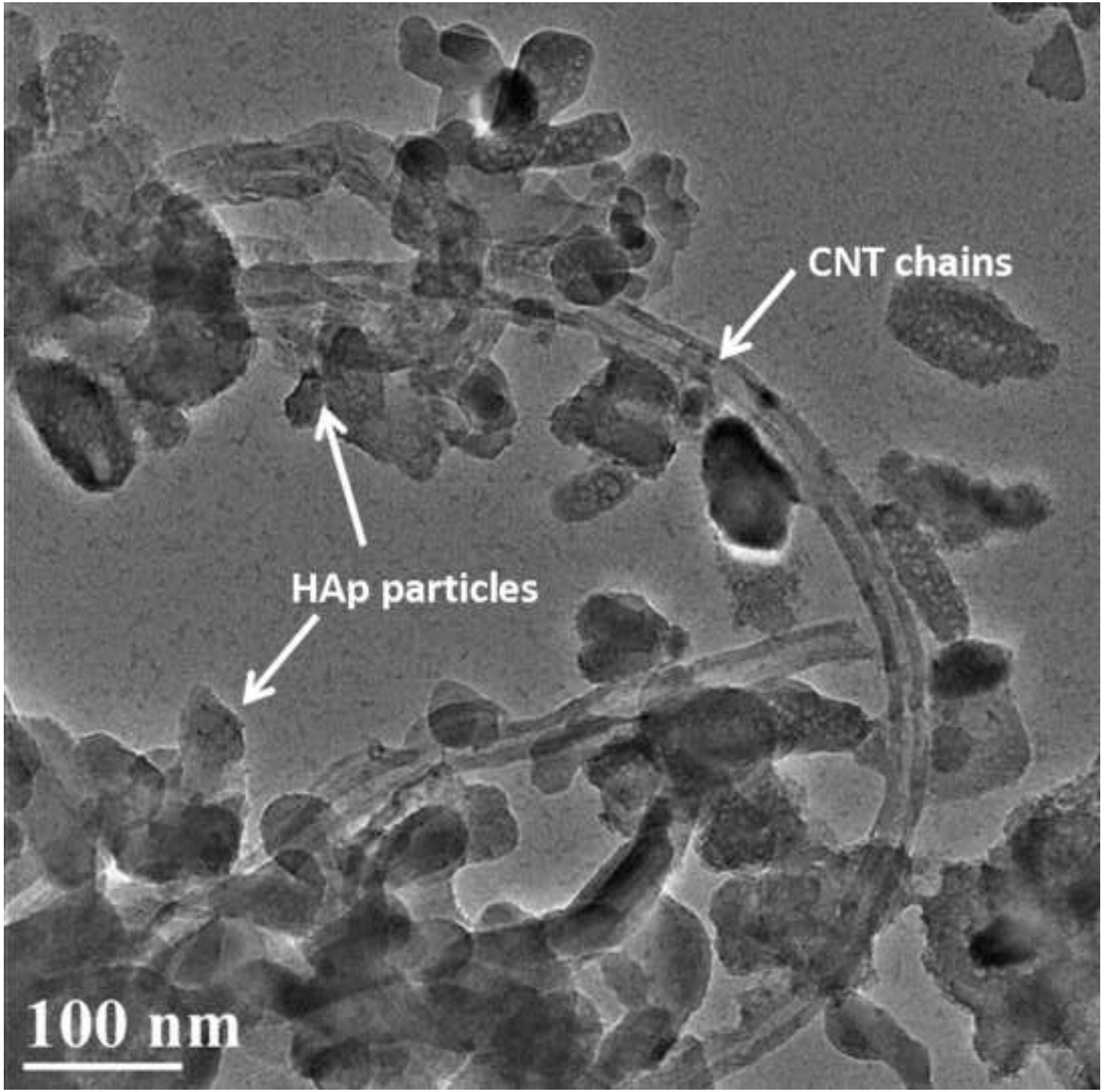

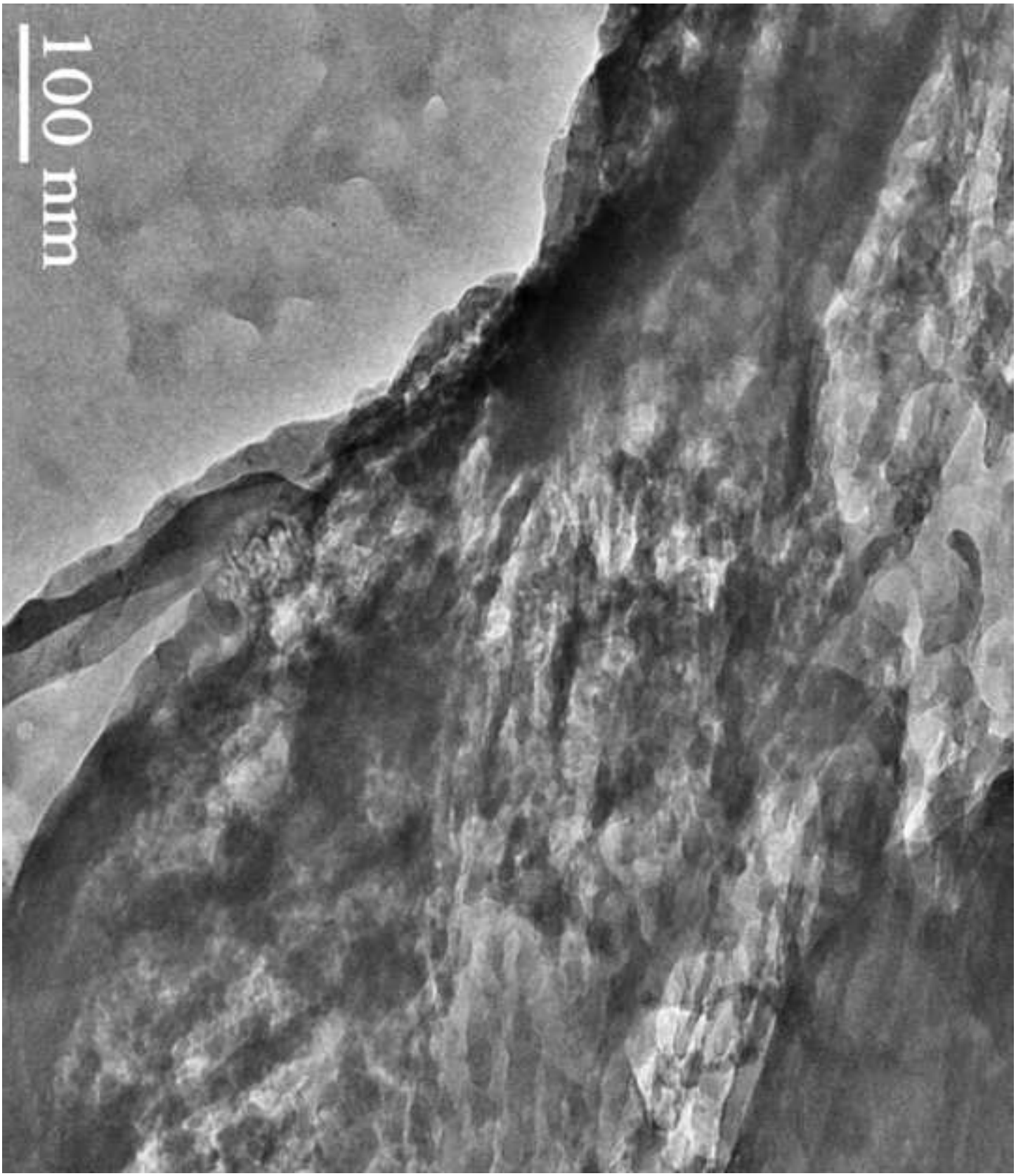

Figure 9d

Figure 10

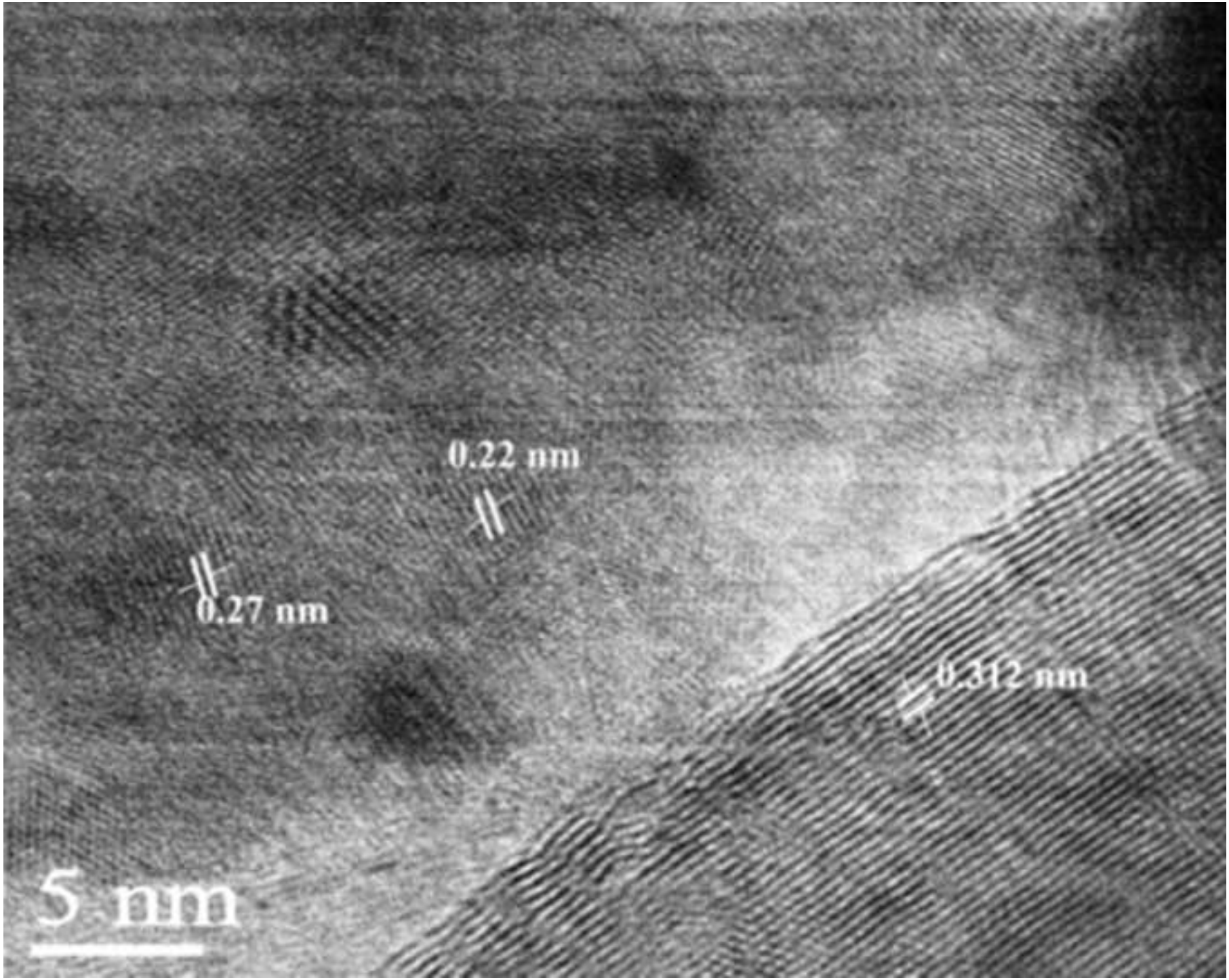

Figure 11

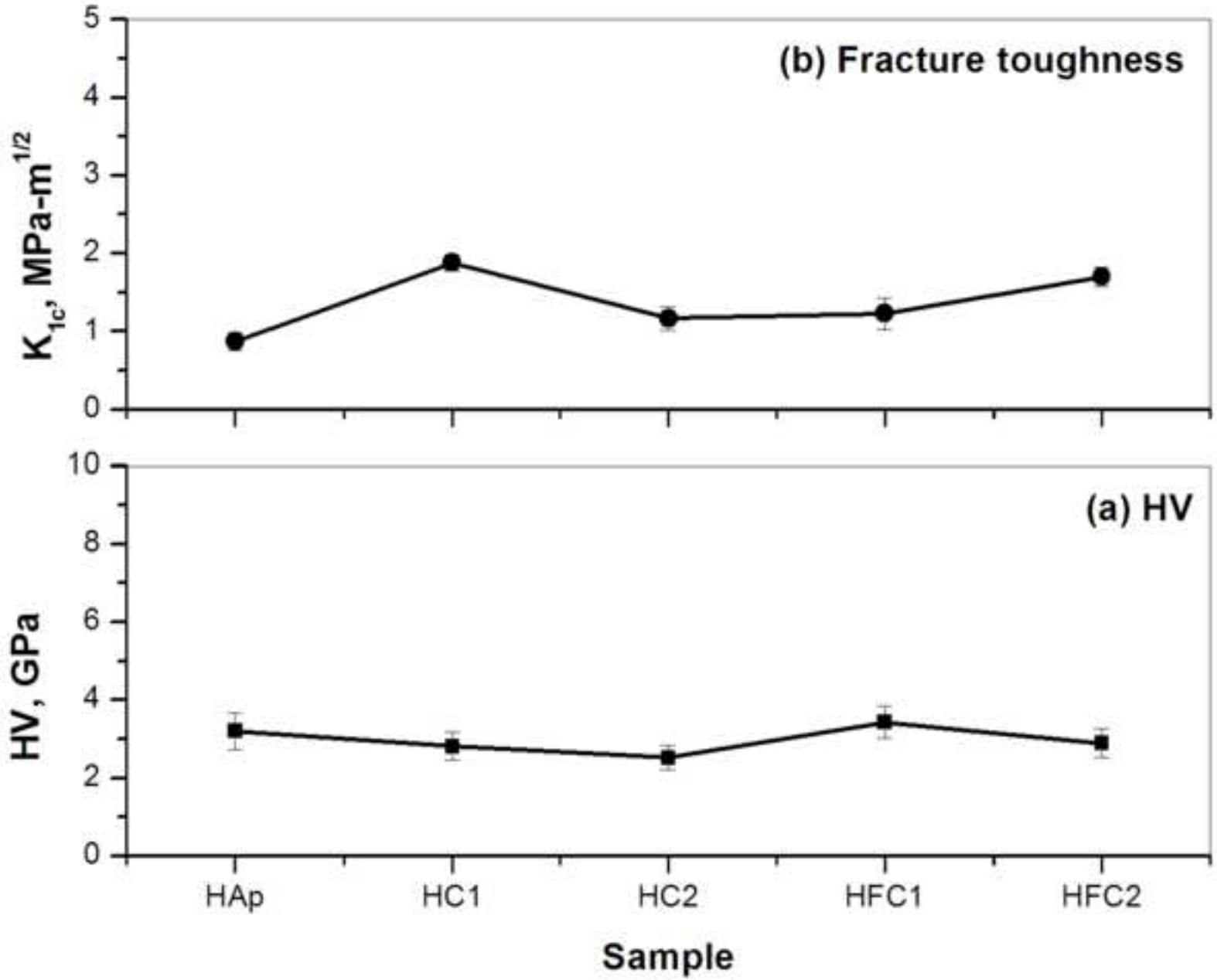

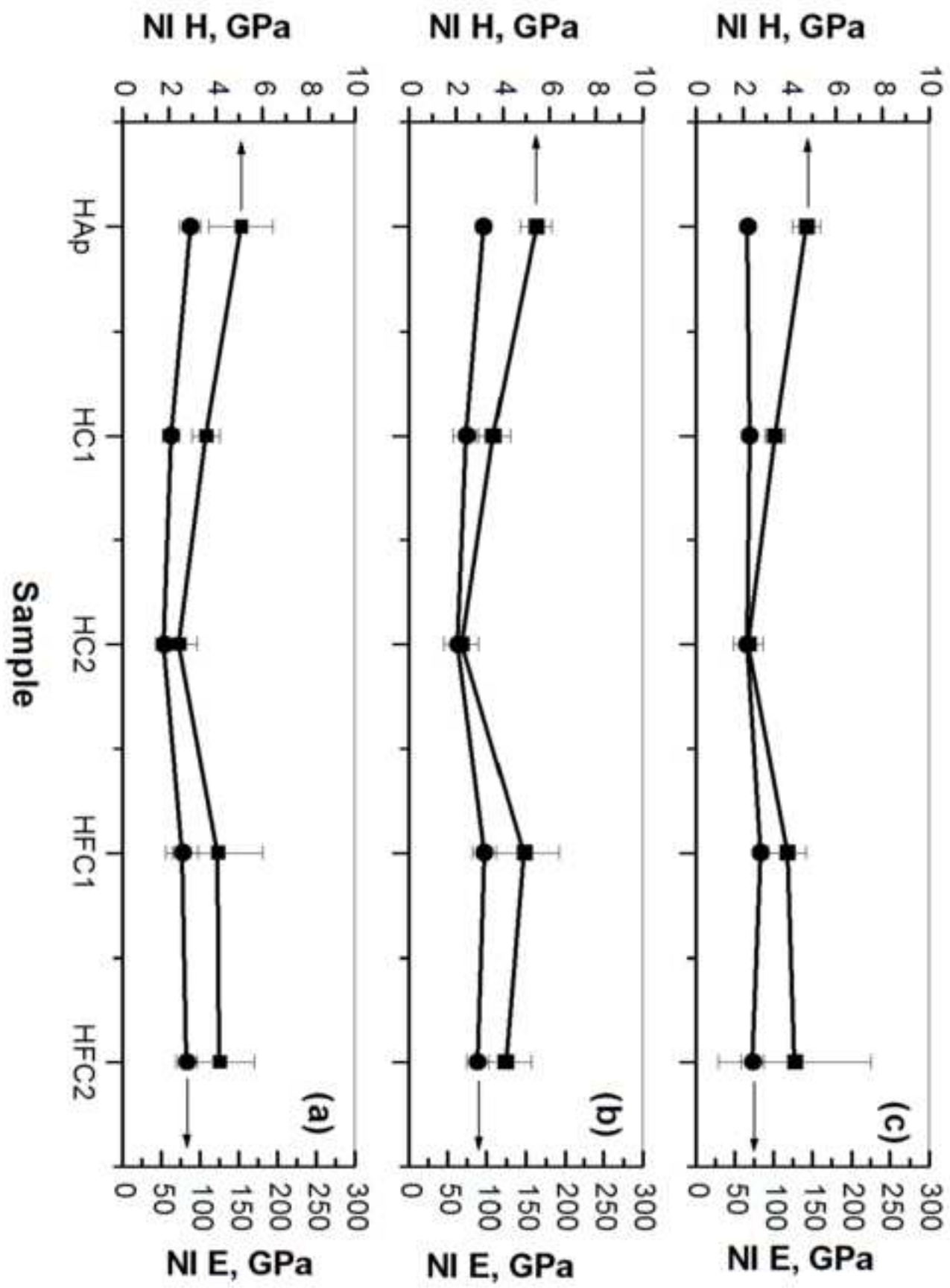

Figure 12

Figure 13